Communication

Angularly Stable Frequency Selective Surface Combined With a Wide-Scan Phased Array

Cristina Yepes, Daniele Cavallo, Erio Gandini, Stefania Monni, Andrea Neto, and Frank E. van Vliet

***Abstract*— A five-layer frequency selective surface (FSS) composed of subwavelength elements with large harmonic rejection bandwidth is presented. The FSS design is based on an equivalent circuit model, where the interlayer interaction is only described with a single transmission line representing the fundamental Floquet wave. A prototype of the designed FSS is fabricated, and the measured response exhibits good stability over a wide conical incidence range up to 45°. The FSS is combined with a wide-scanning connected array of dipoles to implement a phased array with integrated filtering properties. A dispersion analysis is performed to define the distance between the array and the FSS that avoids the propagation of surface waves between the combined structures, allowing to maximize the radiation efficiency. The performance of the array combined with the FSS is experimentally characterized, showing high-order harmonic rejection better than 17 dB over a large bandwidth.**

***Index Terms*— Frequency selective surface (FSS), phased array antennas, spatial filters.**

I. Introduction

Active phased array antennas must comply with stringent requirements in terms of sensitivity to interference caused by other nearby radiating systems, especially in complex platforms, which are populated by an ever-increasing number of sensors and communication systems. Radio frequency (RF) interference can cause a number of issues, e.g., saturation of the array receiver, with consequent loss of sensitivity and missed detections, or increased false alarm rates. This performance degradation can be prevented by implementing frequency selective functions in the antenna panel and RF front end. For this purpose, filters are inserted in the transmit/receive module of the individual antenna elements, although this approach can be problematic due to the limited available physical space.

A possible method to realize compact filters is to use the antenna element itself to perform part of the filtering function, implementing the so-called filtenna concept [1], [2]. An example of a phased array unit cell design with integrated filtering properties was presented in [3]. However, higher harmonic suppression was achieved over a small frequency bandwidth and scanning of the antenna array caused detuning of the filter response.

Another approach to block the undesired radiation is the implementation of frequency selective surfaces (FSSs). The advantage of this latter solution is to alleviate the complexity of the antenna feed structure or the RF front end by reducing the requirements on other filtering stages [4]. Nevertheless, FSSs can also suffer from the appearance of higher order harmonics close to the operational bandwidth and their response can strongly vary with the angle of incidence [5]. FSSs typically consist of one or multiple layers composed of resonant elements arranged in periodic grids [5]. An approach to improve the angular stability is to add additional quarter-wave ($\lambda/4$) dielectric slabs on the two sides of the FSS [5], [6]. However, such a solution leads to electrically thick structures and is not effective in rejecting higher order harmonics.

Recently, an improved concept based on miniaturized-element FSS (MEFSS) was proposed in [7]. This solution consists of a number of layers, each made of a periodic arrangement of subwavelength elements. Considering that the elements are much smaller than the wavelength, the behavior of each layer can be represented as a shunt impedance (capacitive or inductive), with respect to a plane-wave propagation, over a large frequency range [8]. The design of an MEFSS suppressing harmonic responses was presented in [9], and achieved stable behavior for oblique incidence in the principal planes. The thickness was electrically small, less than $\lambda/10$, rather than a multiple of $\lambda/4$, resulting in lower losses. Nevertheless, in [9] or in other more recent designs [10], the FSS was only characterized and tested under plane-wave illumination.

In this communication, we present the design of a bandpass MEFSS with harmonic rejection properties, and we study the effects of placing it in the close proximity of a phased array antenna. For this purpose, we use the connected array of dipoles developed in [11]. The investigation of the performance of the combined array-MEFSS system is relevant, since the vicinity of the array to the FSS can cause variations of both the FSS response and the array matching or radiation patterns. The distance should be selected such to avoid the propagation of guided modes between the array plane and the FSS within the operational bandwidth.

Another aspect to be taken into account when designing MEFSSs is the tolerance of manufacturing, which can produce significant differences between simulations and measurements [10]. A study of the effects of the fabrication inaccuracies on the performance of the FSS is also presented here. This communication is useful to identify the geometrical parameters that are most critical for the correct prediction of the performance. This information can be used as a guideline for the design of MEFSSs that are more robust against manufacturing errors.

Manuscript received July 21, 2017; revised November 8, 2017; accepted November 26, 2017. Date of publication December 1, 2017; date of current version February 1, 2018. This work was supported in part by the Netherlands Organisation for Applied Scientific Research (TNO) DO-AIO Fund and in part by the TNO V1512 Defense Radar Program. *(Corresponding author: Cristina Yepes.)*

C. Yepes is with the Microelectronics Department of the Electrical Engineering, Mathematics and Computer Science Faculty, Delft University of Technology, 2628 CD Delft, The Netherlands, and also with the Department of Radar Technology, Netherlands Organisation for Applied Scientific Research, 2597 AK The Hague, The Netherlands (e-mail: c.yepesjulia@tudelft.nl)

D. Cavallo and A. Neto are with the Microelectronics Department of the Electrical Engineering, Mathematics and Computer Science Faculty, Delft University of Technology, 2628 CD Delft, The Netherlands.

E. Gandini and S. Monni are with the Department of Radar Technology, Netherlands Organisation for Applied Scientific Research, 2597 AK The Hague, The Netherlands.

F. E. van Vliet is with the Department of Radar Technology, Netherlands Organisation for Applied Scientific Research, 2597 AK The Hague, The Netherlands, and also with the Center for Array Technology, University of Twente, 7522 NB Enschede, The Netherlands.

Color versions of one or more of the figures in this communication are available online at http://ieeexplore.ieee.org.

Digital Object Identifier 10.1109/TAP.2017.2778768

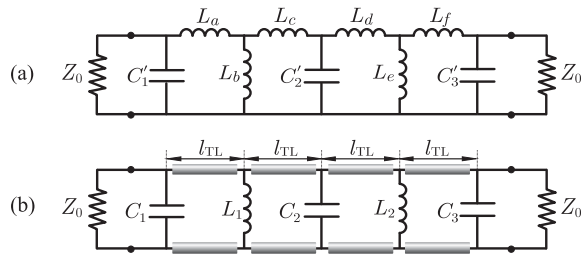

Fig. 1. (a) L–C filter circuit and (b) filter topology with sections of transmission line.

TABLE I

VALUES OF THE LUMPED ELEMENTS AND THE TRANSMISSION LINES

C_1	C_2	C_3	L_1	L_2	l_{TL}, h_{diel}
235 fF	455 fF	235 fF	2.03 nH	2.03 nH	3.175 mm

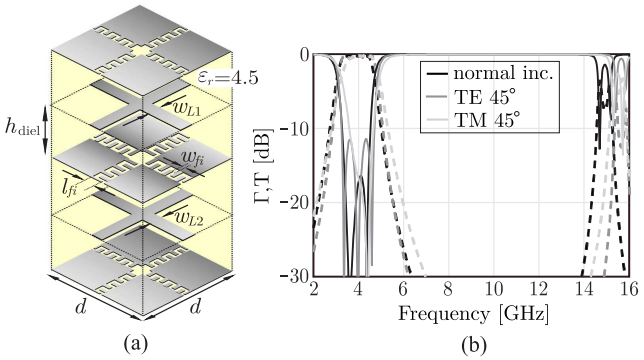

Fig. 2. (a) FSS unit cell realizing the equivalent circuit of Fig. 1(b). (b) Reflection (solid line) and transmission (dashed line) coefficients of the FSS for broadside, 45° TE and TM oblique incidence.

TABLE II

GEOMETRICAL PARAMETER (IN mm) OF THE FSS UNIT CELL

w_{fi}	l_{f1}	l_{f2}	l_{f3}	w_{L1}	w_{L2}	d	h_{diel}
0.15	0.46	0.92	0.46	0.17	0.17	4.2	3.175

II. FREQUENCY SELECTIVE SURFACE DESIGN

In this section, the simulated performance of the multilayer FSS is reported. The design of the FSS is similar to the one presented in [13], though the target bandwidth is more than 20%, centered around another frequency (4 GHz). The design steps in [12] are used to design the three-pole Chebyshev bandpass filter topology in Fig. 1(a). The final equivalent circuit is depicted in Fig. 1(b), where the series inductances and part of the shunt capacitances are replaced by short transmission lines. The values of the shunt lumped components and the length of the transmission lines (assuming a relative permittivity of $\varepsilon_r = 4.5$) are shown in Table I.

The capacitive and inductive layers can be realized with metallic periodic meshes, and the transmission line sections are represented by dielectric slabs separating the metal layers, as shown in Fig. 2(a). To achieve the needed values of capacitance, interdigital capacitors are implemented.

The unit cell period is $d = 4.2$ mm, equivalent to $\lambda_0/18$, where λ_0 is the wavelength at 4 GHz. The geometrical parameters for the capacitive and inductive layers of the FSS unit cell are presented in Table II. The metal layers are separated by dielectric spacers of permittivity $\varepsilon_r = 4.5$ and thickness $h_{diel} = 3.175$ mm. The overall height of the structure is $\lambda_0/6$. The minimum gap width in the interdigitated capacitances is kept as 0.15 mm, which is compatible with the standard printed circuit board (PCB) technology.

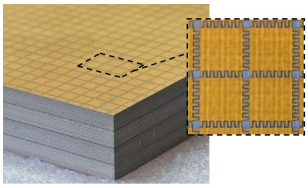

Fig. 3. Photograph of the manufactured FSS.

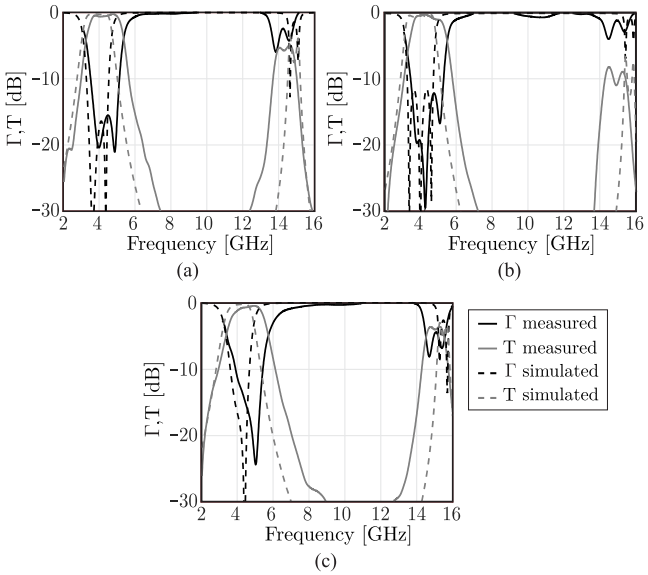

Fig. 4. Comparison between simulated and measured Γ and T of the FSS for (a) normal, (b) TE 45°, and (c) TM 45° plane-wave incidence.

Fig. 2(b) shows the simulated reflection (Γ) and transmission (T) coefficients for normal incidence and transverse electric (TE) and transverse magnetic (TM) oblique incidence at 45°. In the simulations, bonding layers with relative permittivity $\varepsilon_r = 2.32$ and thickness 38.1 μm are included. It can be noted that Γ is lower than -10 dB over a bandwidth of about 23% centered at 4 GHz. The higher order harmonics are rejected up to 14.3 GHz, with $T < -20$ dB.

III. ANALYSIS OF THE PROTOTYPE FSS

The designed FSS has been manufactured, and a photograph of the prototype is shown in Fig. 3. The overall dimensions of the fabricated panel are 445.2×400 mm^2. The metal layers are made of 18 μm-thick copper. The dielectric material is Nelco 9450, with relative permittivity $\varepsilon_r = 4.5$, dissipation factor of $\tan\delta = 0.003$, and thickness 3.175 mm. The material used for the bonding layers is Arlon Cuclad 6250, with a thickness of 38.1 μm and a relative permittivity of $\varepsilon_r = 2.32$.

With respect to the measurements of the reflection coefficient, the FSS is located in the far field of a transmitting horn antenna, and the specular reflection is measured at different angles by a receiving horn also in the far field. The reflected power is then normalized to the power reflected by a metal plate with the same dimensions of the FSS. For the transmission coefficient, the two horns are aligned in the direction of maximum gain, and the FSS is placed in the middle, with different orientations. The transmitted power in the presence of the FSS is then normalized by the power measured in the absence of the FSS.

Γ and T for broadside, TE, and TM oblique incidence at 45° are shown in Fig. 4, comparing CST simulations with measurements.

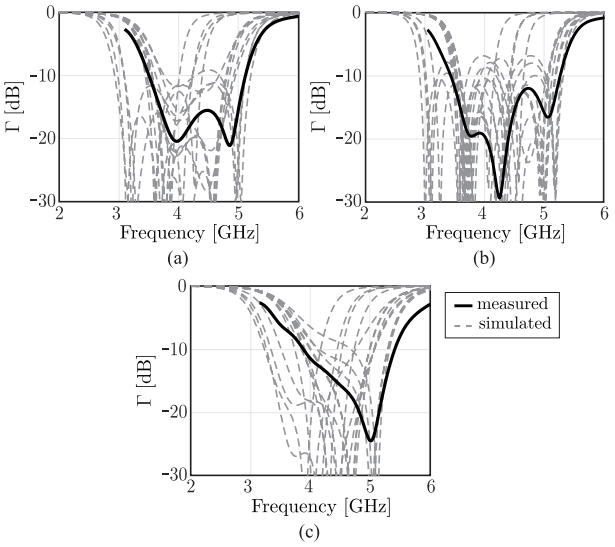

Fig. 5. Variation of the reflection coefficient (Γ) of the FSS when manufacturing tolerances are included for (a) normal, (b) TE 45°, and (c) TM 45° plane-wave incidence.

The thickness of the metal and bonding layers is also included in the simulations. It can be noted that the measured results are shifted by 10% toward higher frequency and the bandwidth is enlarged compared with the simulations. The measured response is characterized by a central frequency of $f_0 = 4.5$ GHz and 27% bandwidth. Moreover, the position of the higher order harmonic is shifted toward lower frequencies, at 13.7 GHz, but still above $3f_0$.

It should also be mentioned that the values of the measured reflection coefficient slightly exceed unity at some frequencies, within the FSS rejection band. This is due to inaccuracies of the measurement setup in terms of alignment, exact positioning of the FSS and the metal plate, as well as reflections from the supporting structures utilized for the FSS, the metal plate, and the horns.

A. Tolerance Study

To explain the discrepancy observed between measurements and predictions, an analysis of the manufacturing tolerances is carried out. The study is based on expected tolerances, as specified by the PCB manufacturer, as well as on inspections of the actual geometrical dimensions performed with a microscope.

The widths of the slots and the metal strips were measured in several areas of the FSS, as well as the metal thickness (through a Dektak surface profiler). It was found that the variations of design parameters are within the following intervals: ± 2 μm for the metal thickness and ± 20 μm for the widths of slots and metal strips. Additional variations of the thickness of the dielectric slabs (± 100 μm) and their relative dielectric permittivity (± 0.1) were considered.

The results of the parametric investigation are summarized in Fig. 5, which shows a group of simulated curves, obtained with different combinations of the varying parameters. The simulations, including the tolerance, explain the frequency shift observed in the measurements. Slightly lower values of Γ and slower roll-off are observed around 6 GHz for TM incidence at 45°, compared with simulations. This might due to additional losses (e.g., from the absorbing material used to create a window in front of the FSS) and to the previously mentioned inaccuracies of the normalization procedure for Γ.

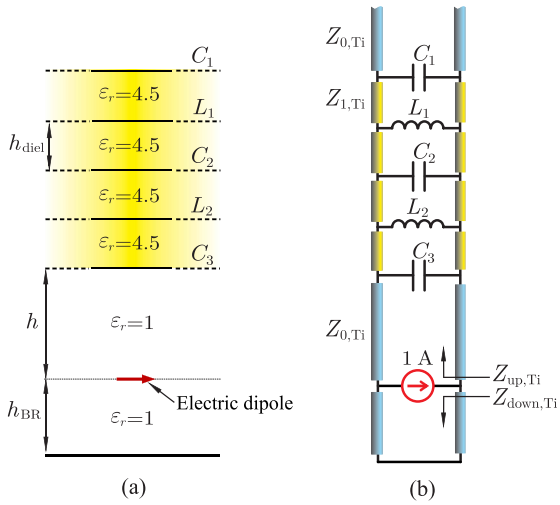

Fig. 6. (a) Geometry and (b) transmission line model used to calculate modes propagating within the stratification.

Moreover, the effect of each parameter has been investigated individually. The findings of this analysis can be summarized as follows.

1) The width of the interdigital capacitance is the most sensitive parameter and is responsible for the shift in the frequency of the FSS bandwidth.
2) The thickness variations of the dielectric slabs are largely responsible for the shift in the frequency of the spurious harmonic.
3) The enlargement of the bandwidth is primarily caused by the variation of the track width in the inductive layer.

IV. Performance of the FSS in Combination With a Connected Array of Dipoles

The objective of this section is to analyze the performance of the MEFSS in the presence of a phased array antenna. To this aim, the connected array prototype developed in [11] is used. This antenna array is composed of 7×7 elements and can scan within a $\pm 45°$ range for every azimuth angle over the frequency band of 3–5 GHz. One of the benefits of using connected arrays is that the antenna impedance is stable over a large frequency range, including the FSS bandwidth, so that the antenna represents a constant loading for the FSS within the operating bandwidth [13].

A dispersion analysis is carried out to determine at what distance from the array the FSS should be located to avoid the occurrence of surface waves within the bandwidth of operation.

A. Dispersion Analysis

To investigate the modes propagating within the layered medium, we consider the simplified geometry in Fig. 6(a): this represents an elementary electric dipole located at distance h from the FSS and at distance h_{BR} from a backing reflector, fixed to 18.9 mm as in [11]. The spectral Green's function can be related to the voltage and current solutions of the transmission line shown in Fig. 6(b) for the TE and TM modes. The characteristic impedances of the transmission lines are $Z_{n,\text{TE}} = \zeta_n k_n / k_{zn}$ and $Z_{n,\text{TM}} = \zeta_n k_{zn} / k_n$ for the TE and TM modes, respectively, where the subscript n is 0 for free space and 1 for the dielectric, ζ_n and k_n are the medium impedance and the wavenumber of the corresponding material, and $k_{zn} = (k_n^2 - k_\rho^2)^{1/2}$. The elementary dipole is represented by a shunt current source with unit amplitude.

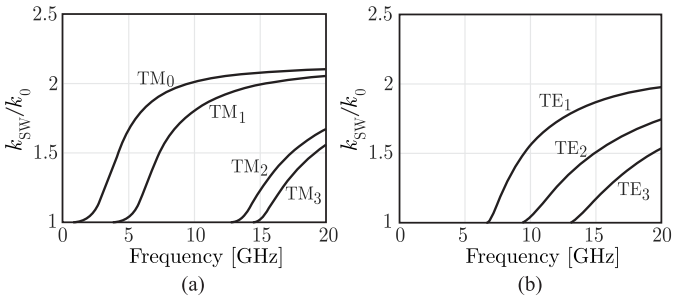

Fig. 7. Dispersion diagram of the surface wave poles for (a) TM modes and (b) TE modes.

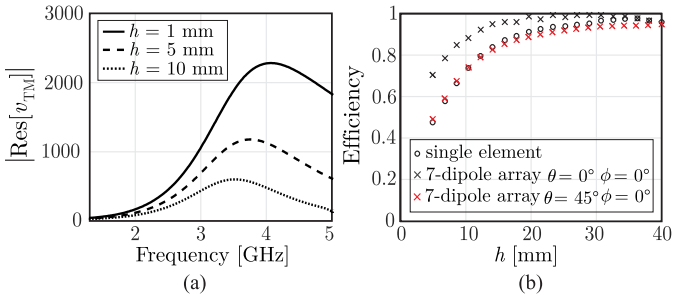

Fig. 8. (a) Residue correspondent to the TM$_0$ mode for different distances. (b) Simulated radiation efficiency of a single short dipole and an array of seven short dipoles in the presence of the stratification in Fig. 6(a) as a function of the distance h.

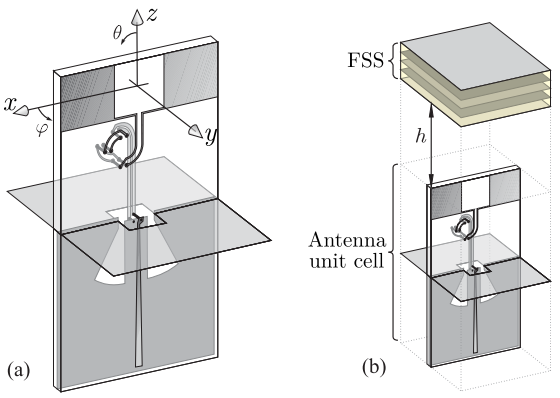

Fig. 9. (a) Connected dipole unit cell. (b) 3-D view of the MEFSS and the connected dipole array combined.

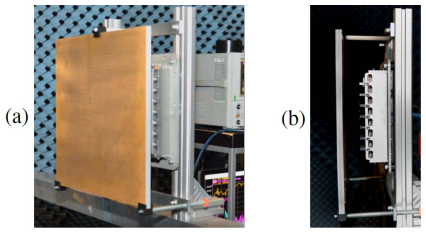

Fig. 10. Photographs of the manufactured MEFSS in combination with the connected array of dipoles. (a) Front view. (b) Side view.

The propagating surface wave modes can be found by solving the following dispersion equation:

$$D(k_\rho) = Z_{\text{up,Ti}}(k_\rho) + Z_{\text{down,Ti}}(k_\rho) = 0 \tag{1}$$

where the impedances $Z_{\text{up,Ti}}$ and $Z_{\text{down,Ti}}$ are defined as in Fig. 6(b), and the subscript Ti can refer to either TE or TM. The zeros of (1) are found numerically with an iterative Newton method. The resulting TM and TE surface waves poles are shown in the dispersion diagram in Fig. 7 as a function of the frequency.

By restricting the observation to the range 3–5 GHz, in which the antenna array operates, there is only one dominant TM surface wave. We observed that the position of this polar singularity is not dependent on the distance h, as it is related to propagation in the dielectric. However, the residue associated with the pole varies with the distance, and thus, the amount of power carried by this wave can change. To clarify this aspect, Fig. 8(a) shows the residue of the voltage v_{TM} at the generator $\text{Res}[v_{\text{TM}}] = N(k_{\text{SW}})/D'(k_{\text{SW}})$ for different values of h, where $N(k_\rho) = Z_{\text{up,TM}}(k_\rho) \times Z_{\text{down,TM}}(k_\rho)$ and D' represent the derivative of the function in (1). The simulated radiation efficiency of a short dipole in the presence of the FSS was also simulated with CST microwave studio and reported in Fig. 8(b) at 4 GHz, as a function of the distance h. Also, the efficiency of a linear array of seven collinear short dipoles scanning at broadside is shown, resulting in a higher efficiency. However, when the array scans in the direction of the surface wave mode ($\theta = 45°$ $\phi = 0°$), the efficiency is reduced. The plotted efficiency is defined as $P_{\text{rad}}/(P_{\text{rad}} + P_{\text{SW}})$, where P_{rad} is the total power radiated to free space and P_{SW} is the power launched into surface waves. From Fig. 8(b), it can be observed that the efficiency increases with the distance h and remains above 90% for all distances in the range of 12.5–40 mm for broadside, and in the range of 23.5–40 mm scanning at $\theta = 45°$ $\phi = 0°$.

Moreover, when the array of connected dipoles is considered in the presence of the layered medium, the distance should be still large enough to assume that only the fundamental Floquet mode is dominating the interaction between the dipoles and the FSS, so that reactive coupling can be neglected. For this reason, a distance of around half wavelength at 4 GHz (37.5 mm) is considered. This value corresponds to 93% efficiency for a short dipole radiating in the presence of the FSS, as can be seen in Fig. 7(b).

B. Matching Properties of the Combined Array/MEFSS

Fig. 9(a) shows a 3-D view of the connected dipole unit cell from [11]. The dipole arms are connected to a loop structure that has the purpose of rejecting the common-mode currents. The feeding structure is then connected to a sleeve balun under the backing reflector, to implement the transition from differential to single-ended transmission line. Fig. 9(b) displays the same dipole element cascaded with the idealized FSS located at distance $h = 37.5$ mm from the top of the dipole. The simulated values of capacitive and inductive layers of the FSS were modified with respect to the ones in Table II, so that the simulations are representative of the measurements presented in Section III-A.

The connected array prototype developed in [11] is used to experimentally evaluate the effects of the MEFSS in the proximity of an array. Photographs of both structures combined are shown in Fig. 10.

In Fig. 11, the simulated and measured active voltage standing wave ratio (VSWR) of the standalone connected-dipole array and the combination of the array with the FSS are shown, for broadside and scanning up to 45° in the E-plane and H-plane. The bandwidth defined as VSWR < 3 is highlighted in all the figures. By comparing the two simulated results [see Fig. 11(a) and (b)], it is evident that the presence of the FSS reduces the bandwidth of the antenna from 4 to 5 GHz while keeping good levels of matching. Narrow resonances occur between 5 and 5.5 GHz also in the presence of the FSS. However, these resonances are mainly due to the

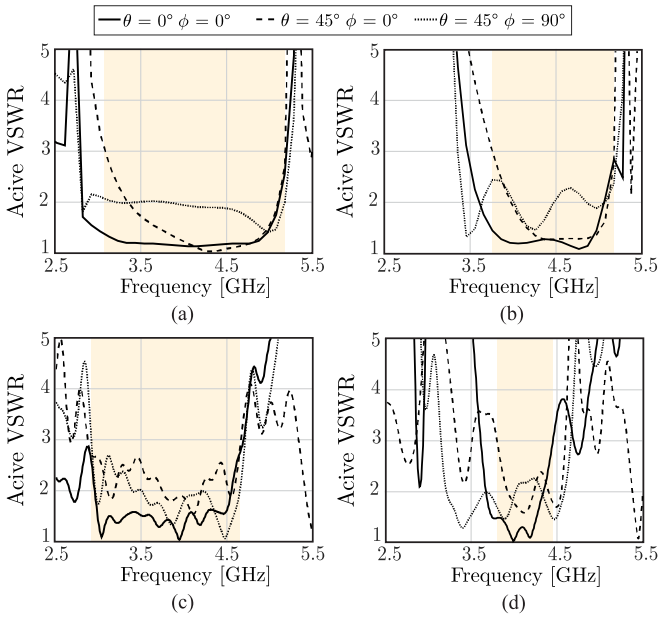

Fig. 11. Simulated active VSWR of (a) array alone and (b) with the FSS; measured active VSWR of (c) array alone and (d) with the FSS.

limited bandwidth of the dipole feed structure. Outside the range of 3–5 GHz, the feeding lines of the dipoles do not exhibit good matching characteristics, and the common-mode rejection structure is no longer effective. Similar effects can be observed from the measured results in Fig. 11(c) and (d). The presence of the FSS reduces the bandwidth, compared with the array alone. It can be noted that measured upper limits of the bandwidth are lower than the simulated ones, with and without the FSS. This effect is due to a mismatch of the SMA connector transition for frequency above 4.5 GHz, which is not accounted for in the simulations.

C. Gain and Patterns of the Combined Array/MEFSS

The transmission coefficients between a horn located in the far field and the central element of the connected array have been measured, with and without the FSS. The active element gain, normalized to the maximum directivity of the unit cell aperture ($4\pi A/\lambda^2$), is plotted in Fig. 12 for broadside radiation and scanning at 45° in the E- and H-planes. It can be appreciated that, within the operational bandwidth of the FSS (highlighted in Fig. 12), the element gain with the FSS is very close to that of the antenna alone. In the frequency range from 6 to 18 GHz, the gain of the antenna with the FSS is 17 dB lower for broadside and scanning up to 45° in the two main planes.

Oscillations of around 2–3 dB are observed within the FSS passband, and they are mainly due to truncation effects of the finite array. Indeed, the period of these fluctuations can be related to the distance between the measured element and the edges of the array. Time gating with narrower windows would eliminate the oscillations; however, this was not applied to account for the multiple reflections that might occur between the FSS and the array.

In addition, the measured normalized active element patterns in the E- and H-planes for the case of the antenna alone and in combination with the FSS are shown in Fig. 13. Both copolar and cross-polar components are shown at the frequency of 4 GHz. The normalized copol for the antenna alone and in combination with the FSS is similar between −45° and 45° angles where the FSS is working. The normalized X-pol pattern is below −15 dB in the E-plane and −18 dB in the H-plane for both configurations. Measurements for the D-plane were not possible due to supporting structure limitations. Nevertheless, the X-pol level for $\phi = 45°$ and $\theta = 45°$ was simulated (see Fig. 14), being lower than −10 dB within the FSS bandwidth.

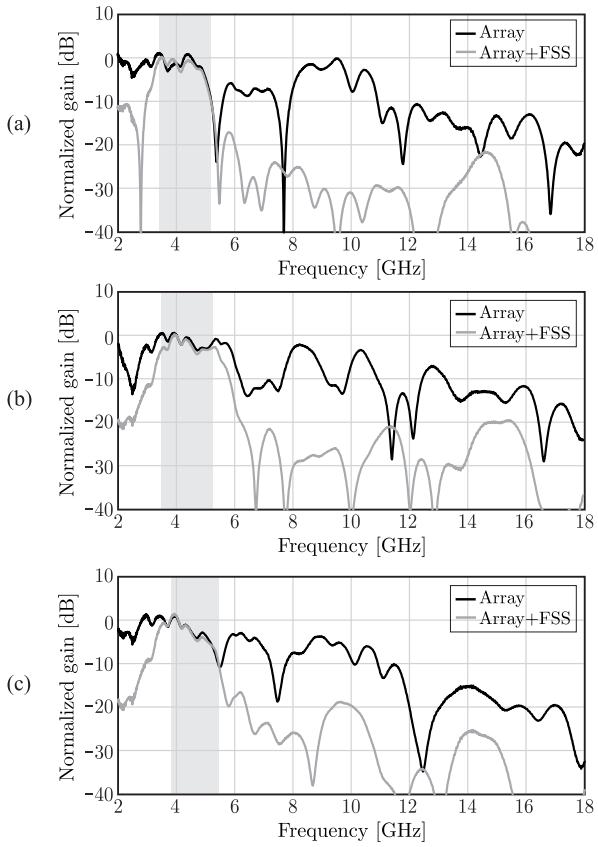

Fig. 12. Measured active element gain normalized by the ideal directivity of the unit cell aperture, with and without the FSS for (a) broadside, (b) E-plane, and (c) H-plane at 45°.

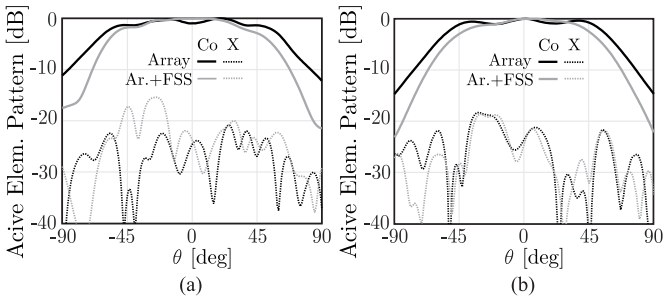

Fig. 13. Copolar (Co) and cross-polar (X) measured normalized active element patterns in (a) E-plane and (b) H-plane at 4 GHz.

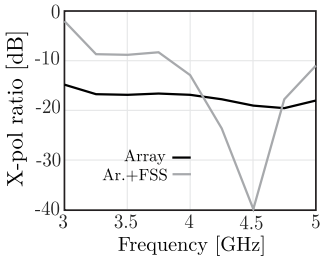

Fig. 14. Simulated X-pol ratio for the array when scanning to $\theta = 45°$ and $\phi = 45°$, with and without the FSS.

V. Conclusion

An MEFSS was designed, fabricated, and tested. Measured results showed a bandwidth of 27% around the central frequency of 4.5 GHz. The unit cell size has the dimensions of 4.2×4.2 mm^2 and a total height of $\lambda_0/5.2$, where λ_0 is the wavelength at 4.5 GHz. A large rejection of higher order harmonics is achieved with the first harmonic at the frequency of 13.7 GHz, with a transmission coefficient lower than -20 dB.

To investigate the interaction with wideband antennas with a wide scanning range, the MEFSS was combined with a connected dipole array antenna. The minimum distance between the antenna and the FSS for which no resonances or surface waves propagation occur was investigated through a dispersion analysis. When combining both structures, it can be appreciated that the response within the FSS passband agrees well with the one of the antennas alone, while a broadband out-of-band rejection, better than 17 dB, is measured from 6 to 18 GHz and for scanning up to 45° in the main planes. The FSS is, therefore, effective in rejecting out-of-band sources of interference over a broad frequency range. Measured active element patterns for the E- and H-planes show a slight decrease in beamwidth when the FSS is included.

Acknowledgment

The authors would like to thank F. Nennie, M. Bruijn, R. Bolt, R. Boekema, D. Thoen, and P. Aubry for their contribution to the support manufacturing and the measurement campaign.

References

[1] A. Abbaspour-Tamijani, J. Rizk, and G. Rebeiz, "Integration of filters and microstrip antennas," in *Proc. IEEE Antennas Propag. Soc. Int. Symp.*, vol. 2. Jun. 2002, pp. 874–877.

[2] T. Le Nadan, J. P. Coupez, and C. Person, "Optimization and miniaturization of a filter/antenna multi-function module using a composite ceramic-foam substrate," in *IEEE MTT-S Int. Microw. Symp. Dig.*, vol. 1. Anaheim, CA, USA, Jun. 1999, pp. 219–222.

[3] L. Cifola, D. Cavallo, G. Gerini, and A. Morini, "Compact design of a planar filtering antenna array including a frequency selective common-mode rejection module," in *Proc. IEEE Int. Symp. Antennas Propag.*, Chicago, IL, USA, Jul. 2012, pp. 1–2.

[4] F. Bayatpur and K. Sarabandi, "Miniaturized FSS and patch antenna array coupling for angle-independent, high-order spatial filtering," *IEEE Microw. Wireless Compon. Lett.*, vol. 20, no. 2, pp. 79–81, Feb. 2010.

[5] B. A. Munk, *Frequency Selective Surfaces: Theory and Design*. New York, NY, USA: Wiley, 2000.

[6] S. Monni, A. Neto, G. Gerini, F. Nennie, and A. Tijhuis, "Frequency-selective surface to prevent interference between radar and SATCOM antennas," *IEEE Antennas Propag. Lett.*, vol. 8, pp. 220–223, Apr. 2009.

[7] M. Al-Joumayly and N. Behdad, "A generalized method for synthesizing low-profile, band-pass frequency selective surfaces with non-resonant constituting elements," *IEEE Trans. Antennas Propag.*, vol. 58, no. 12, pp. 4033–4041, Dec. 2010.

[8] L. B. Whitbourn and R. C. Compton, "Equivalent-circuit formulas for metal grid reflectors at a dielectric boundary," *Appl. Opt.*, vol. 24, no. 2, pp. 217–220, Jan. 1985.

[9] S. M. A. M. H. Abadi, M. Li, and N. Behdad, "Harmonic-suppressed miniaturized-element frequency selective surfaces with higher order bandpass responses," *IEEE Trans. Antennas Propag.*, vol. 62, no. 5, pp. 2562–2571, May 2014.

[10] M. Gao, S. M. A. M. H. Abadi, and N. Behdad, "A dual-band, inductively coupled miniaturized-element frequency selective surface with higher order bandpass response," *IEEE Trans. Antennas Propag.*, vol. 64, no. 8, pp. 3729–3734, Aug. 2016.

[11] D. Cavallo, A. Neto, G. Gerini, A. Micco, and V. Galdi, "A 3- to 5-GHz wideband array of connected dipoles with low cross polarization and wide-scan capability," *IEEE Trans. Antennas Propag.*, vol. 61, no. 3, pp. 1148–1154, Mar. 2013.

[12] G. L. Matthaei, L. Young, and E. M. T. Jones, *Microwave Filters, Impedance-Matching Networks, and Coupling Structures*. Norwood, MA, USA: Artech House, 1980.

[13] C. Yepes, D. Cavallo, A. Neto, E. Gandini, S. Monni, and F. E. van Vliet, "Sub-wavelength frequency selective surface design for improved antenna array out-of-band rejection," in *Proc. IEEE Int. Symp. Phased Array Syst. Technol.*, Waltham, MA, USA, Oct. 2016, pp. 1–5.